

**HYDRAULIC STIMULATION OF NATURAL FRACTURES AS REVEALED BY
INDUCED MICROEARTHQUAKES,
CARTHAGE COTTON VALLEY GAS FIELD, EAST TEXAS**

James T. Rutledge and W. Scott Phillips

Los Alamos National Laboratory
Mail Stop D443
Geophysics Group
Seismic Research Center

jrutledge@lanl.gov
wsp@lanl.gov
<http://www.ees11.lanl.gov/microeq>

Presented at the 71st Annual Meeting, Society of Exploration Geophysicists
Submitted March, 2001

Issued:
Geophysics, Vol. 68, (March-April, 2003), 441-452.

LAUR# 01-1204

ABSTRACT

We produced a high-resolution microseismic image of a hydraulic fracture stimulation in the Carthage Cotton Valley gas field of east Texas. We improved the precision of microseismic event locations 4-fold over initial locations by manually repicking the traveltimes in a spatial sequence, allowing us to visually correlate waveforms of adjacent sources. The new locations show vertical containment within individual, targeted sands, suggesting little or no hydraulic communication between the discrete perforation intervals simultaneously treated within an 80-m section. Treatment (i.e., fracture-zone) lengths inferred from event locations are about 200 m greater at the shallow perforation intervals than at the deeper intervals. The highest quality locations indicate fracture-zone widths as narrow as 6 m. Similarity of adjacent-source waveforms, along with systematic changes of phase amplitude ratios and polarities, indicate fairly uniform source mechanisms (fracture plane orientation and sense of slip) over the treatment length. Composite focal mechanisms indicate both left- and right-lateral strike-slip faulting along near-vertical fractures that strike subparallel to maximum horizontal stress. The focal mechanisms and event locations are consistent with activation of the reservoir's prevalent natural fractures, fractures that are isolated within individual sands and trend subparallel to the expected hydraulic fracture orientation (maximum horizontal stress direction). Shear activation of these fractures indicates a stronger correlation of induced seismicity with low-impedance flow paths than is normally found or assumed during injection stimulation.

INTRODUCTION

The volume of rock stimulated by hydraulic fracturing can be imaged by locating microearthquakes induced by the injection (Albright and Pearson, 1982). The microseismic source locations yield the stimulated volume's orientation, length, and height as well as its growth characteristics, information used to calibrate fracture models, improve treatment designs, and guide well placements for optimizing field drainage. In this paper we apply a high-precision location technique to improve the image resolution of a hydraulic fracture treatment in a tight gas sand reservoir in east Texas.

Hydraulic-fracture induced seismicity typically forms an elongated cloud of event locations (e.g., House, 1987; Jones et al., 1995; Warpinski et al., 1995; Phillips et al., 1998). The dominant source mechanism is shear slip, which is induced by elevated pore pressure reducing normal stress along pre-existing fractures (Pearson, 1981). Slip may also occur near the tips of created fractures due to large shear stresses generated by tensile opening (Sneddon, 1946). Since shear slip can be triggered by small pore-pressure increases relative to crack-opening pressure, we expect the microseismic events to extend into the rock, beyond the opened hydraulic-fracture lengths and widths (Evans et al., 1999). The seismic cloud thereby represents shear stress released on surrounding fractures that are favorably oriented for slip. This interpretation has been supported by stress and focal-mechanism information (Fehler, 1989; Cornet and Yin, 1995; Roff et al., 1996; Moriya et al., 2002) and inferred from the development of the seismic cloud's length and width (Warpinski et al., 1995; Phillips et al., 1998; Cornet, 2000). By intersecting and extending beyond the created hydraulic fractures, shear fractures may form significant components of the fracture-drainage network (Hopkins et al., 1998; Tezuka and Niitsuma, 2000; Evans and Jones, 2001). Moreover, the induced shear slip will result in the mismatch of rough fracture surfaces and create permeability by self-propping of natural fractures (Brown and Bruhn, 1998).

Details on how a treatment interacts with and affects a reservoir's natural fractures cannot be readily gleaned from the seismic cloud. Routine event locations provide blurry images of the fracture system that only outline gross treatment dimensions (Jones and Stewart, 1997; Fehler et al., 2001). It is possible, however, to improve relative source locations and resolve discrete structures within the seismic cloud by extracting more consistent arrival-time picks from correlated waveforms (Moriya et al., 1994; Phillips et al., 1997; Gaucher et al., 1998; Phillips,

2000; Rowe et al., 2002). This technique also aids in determining source (i.e., focal) mechanisms of the induced events (fracture plane orientation and sense of slip) that are otherwise difficult to solve with sparse receiver networks. For example, planar structures resolved by precise location can provide independent slip-plane orientations to constrain the focal mechanism (e.g., Phillips, 2000). The source coverage can also be expanded by grouping events with similar waveforms and solving for a common mechanism of the event group (composite focal mechanisms, e.g., Rutledge et al., 1998).

In May and July, 1997 a consortium of operators and service companies seismically monitored six hydraulic fracture treatments in the Carthage Cotton Valley gas field (Figure 1, Walker, 1997). Mayerhofer et al. (2000) and Urbancic and Rutledge (2000) presented the treatment dimensions and interpretations of fracture development obtained from these microseismic data. By determining precise locations and focal mechanisms, we have taken a detailed look at one of these data sets. We first give a brief overview of the reservoir geology, operational set up, and initial image results. After briefly describing our re-analysis, we compare the new image with the old and present our interpretation.

STRUCTURAL SETTING

The Carthage Cotton Valley field underlies 1000 km² of Panola County, East Texas (Figure 1) and is within the northern Gulf of Mexico basin, a structural province of gently dipping beds, open, periclinal folds, and normal faults attributed to diapiric movement of salt (Laubach, 1988). Gas is produced from multiple, low-permeability sands within an interbedded sequence of sands and shales. Within the immediate study area, the top of the Cotton Valley formation is about 2600 m deep and approximately 325 m thick. Overlying the Cotton Valley is the Travis Peak formation, another thick (~ 450-600 m) interval of productive, tight-gas sands interbedded with mudstones. The Cotton Valley and Travis Peak are believed to be within a normal-faulting stress regime with minimum horizontal stress (S_{hmin}) oriented north-northwest. This inference is based on local Quaternary faulting (Collins et al., 1980), hydraulic fracture stress tests, borehole breakouts and coring-induced fracture orientations (Laubach and Monson, 1988). Predicted hydraulic fracture orientation is vertical, striking east-northeast. Natural fractures and stress-direction indicators in several local boreholes indicate that, within the Travis Peak and Cotton

Valley sand intervals, natural fracture populations are dominated by vertical extension fractures, striking within 10° of the contemporary maximum horizontal stress direction (S_{Hmax}) (Laubach, 1988; Laubach and Monson, 1988; Dutton et al., 1991). Few, if any, natural fractures occur in the intervening shales. Based on the similarity of expected hydraulic fracture trend and natural fracture orientations, Dutton et al. (1991) noted that Cotton Valley hydraulic-fracture treatments would likely access the natural fracture system.

OPERATIONAL SETTING

The treatment and monitor wells are shown in Figure 2. Seismicity was monitored for three completion depth intervals in well CGU21-10; we have re-analyzed the seismic data from the Stage-3 completion (Figures 2 and 3). There were two monitor wells (wells CGU22-09 and CGU21-09, Figure 2). These were completed with 715-m-long (2350 ft) arrays of 48 three-component geophone stations fixed to the outside of 2-7/8-inch production tubing and cemented in place. We refer to the CGU21-09 array as Array-1, and the CGU22-09 array as Array-2 (Figures 2 and 3). Geophone stations were spaced at 15 m (50 ft) intervals. Signals were amplified 60 dB downhole, with an additional 48 dB applied uphole before digitizing the waveforms at a 1-ms sample interval. Details of the instrumentation design and installation are presented in Walker (1997). Several data channels were lost from stations damaged during installation. In Array-1, only four stations survived with all three components operating, all within the upper third of its length. For our analysis we used the subset of 10 stations shown in Figure 3, which take advantage of the arrays' long vertical apertures and provide an adequate redundancy of phase arrival times to uniquely constrain the Stage-3 source depths.

Stage-3 Treatment and Initial Locations

The Stage-3 completion interval is within the Upper Cotton Valley formation. The well casing over this 80-m interval was perforated at six discrete subintervals ranging from 3 to 6 m (10 to 20 ft) that targeted specific productive sand layers. Walker (1997) describes the stratigraphy in detail. Figure 4 shows the fracture treatment data and a histogram of the microearthquake event count. A viscous crosslink gel was pumped during the main portion of the treatment to entrain 229,000 kg of sand proppant into formation. Total fluid volume injected was 1253 m^3 (330,919 gallons).

During the treatment Withers and Dart (1997) recorded 1122 events. Of these, Urbancic and Rutledge (2000) manually picked arrival times for 760 events for which P- and S-phase onsets could be identified. We located 696 of these (Figures 2 and 3) with RMS residuals < 5 ms (the root-mean-square of the observed minus model-computed arrival times for all stations). The median RMS residual is 1.3 ms. The location error ellipsoids have major axes generally oriented horizontal and subparallel to the trend of event locations with a median length of 16 m (± 8 m, Figures 2 and 3). Most of the seismicity defines two distinct depth clusters within the perforated interval. The seismicity also implies some downward growth of the Stage-3 treatment terminating at the upper boundary of the Stage-2 interval; upward growth is contained (Figure 3).

The events are asymmetric about the treatment well with 95% located on the east side, closer to the monitor wells (Figure 2). The distribution is likely due to limited detection range. Figure 5 shows relative magnitudes versus source-receiver distances, which we computed as normalized RMS log-amplitudes, averaged for the first 10 ms of P- and S-wave arrivals from the lower 5 stations of Array-2 (Figure 3). We adjusted the amplitudes for spreading, attenuation (Rutledge, 1998), and radiation pattern determined from composite focal mechanisms (discussed below). The lower bounds of the shaded area represents a symmetric detection threshold about the treatment well, limited by the magnitude-distance threshold along the western trend (Figure 5). The events with magnitudes exceeding the symmetric threshold form comparable event populations on each side of the treatment well. Further, 93% of events east of the treatment well would have been out of detection range had they occurred an equal distance west of the well (Figure 5). Assuming that the small magnitude events were also evenly distributed about the treatment well, we speculate that the treatment resulted in a symmetric fracture zone. Since seismicity west of the treatment well was likely undersampled, we concentrate on the higher-quality and presumably more complete event set east of the treatment well in our re-analysis of the data.

SOURCE LOCATION TECHNIQUE

We determined the event locations shown in Figures 2 and 3 using an iterative, least-squares method (e.g., Aki and Richards, 1980, p. 692-695). The method has been generalized to include directional data, so that misfits of traveltimes and directional data are minimized (Phillips

et al., 1998). Our directional data were receiver-to-source azimuths, determined from the first 6 ms of horizontal-component, P-wave particle motions (Flinn, 1965). The azimuthal data resolved location about the plane of symmetry formed by the two monitor wells. To reduce systematic misfits and improve relative locations, we applied P and S station corrections based on median traveltimes residuals (Frohlich, 1979). We used the random component of misfit to obtain the data uncertainties. That is, traveltimes and azimuthal uncertainties were estimated for each station as the standard deviation of their respective residuals (Table 1). The location error ellipsoids reflect the data uncertainties, the distribution of data types and the station-event geometry; we did not consider possible uncertainty in the velocity model.

To calibrate the velocity model we used a set of primacord shots fired in the treatment well and recorded on both arrays. A perforation-gun subassembly was used to detonate the primacord, and a geophone in the cablehead provided detonation time. A six-layer model, initially based on smoothed P and S sonic logs, was calibrated (Rutledge and Urbancic, 1999) using the shots and the best microearthquake data as input to a joint hypocenter-velocity inversion routine (Phillips et al., 1998).

Improving Locations Through High-Precision Picking

Using the same location method and velocity model, we determined new locations with more precise arrival times. We improved the arrival-times precision by systematically and consistently repicking events with similar waveforms (e.g., Phillips et al., 1997). To compare waveforms, we rotated the 3-component data to P (radial), SH and SV components (Figure 6), assuming straight raypaths from the stations to the initial source locations. We then repicked P- and S-arrival times in east-to-west sequences for three depth intervals defined by the initial locations. This allowed us to visually correlate waveforms of adjacent events. We also upsampled the data from a 1-ms to a 0.2-ms sample interval by interpolating using a finite-impulse-response (FIR) filter. Interpolation improved the visual correlation by removing apparent waveform differences caused by the relatively coarse, initial sampling rate (Figure 7). Because the data were properly anti-alias filtered in the field, the FIR-filter interpolation is a band-limited signal reconstruction, with initial data sampling representing a data compression; no unsubstantiated

information is added in the interpolation process (Vaidyanathan, 1990). Subsample arrival-time precision was obtained from the interpolated data by consistently picking easily identified peaks or troughs within the first half cycle of P- and S-phases (e.g., righthand side of Figure 7). By picking peaks or troughs we avoided the uncertainty of trying to pick phase onsets which varies with signal-to-noise ratio, and by interpolating we reduced the uncertainty of identifying the phase maxima and minima due to coarse sampling.

We used easily identified SH phases (e.g., Figure 6) as reference arrivals for displaying waveforms in identical time windows, allowing quick visual correlation. We were often able to obtain reliable SH picks for all 10 stations shown in Figure 3. We made new P-wave picks only on the lower 5 stations of Array-2 (Figure 3). We did not pick SV because of poor signal-to-noise ratios (e.g., Figure 6). Repicking the events in spatial sequence revealed a similarity of adjacent-source waveforms over the entire treatment length (Figure 8).

RESULTS OF REPICKING

New Locations

The original and new locations east of the treatment well are shown in Figures 9 and 10, respectively. The new locations in Figure 10 show a narrower fracture-zone; repicking reduced the standard deviation of locations about a linear fit by more than a factor of four. In depth view, the new locations show five distinct horizontal bands of events within the treatment interval (Figure 10), banding that cannot be seen in the original locations (Figure 9). On average the arrival-time uncertainties have been reduced by a factor of four (Table 1). The major axes of the location errors are horizontal and subparallel to the fracture trend, as in Figures 2 and 3, but with the average length reduced from 16 m to 4 m (± 8 m to ± 2 m). Average relative depth error is slightly less than ± 1 m. The plan-view changes in event location indicate that the initial location errors are underestimated (Figures 9 and 10). Station coverage is very poor in plan view (Figure 2), providing inadequate arrival-time redundancy. As a result, noisy arrival-time data can be over-fitted, giving residuals that underestimate pick errors.

Focal Mechanism Solutions

The similarity of waveforms along the event trend and a change in P-polarities occurring about 270 m east of the treatment well (Figure 8), suggest that a common focal mechanism occurs over the entire length of the fracture system. Waveform character is generally dominated by large-amplitude SH phases (e.g., Figure 6). Proceeding along the treatment length, the sense of P-polarity change near the 270-m distance is correlated with SH polarity. For example, events with negative SH polarity, have P polarities changing from dilational to compressional proceeding eastward across the 270-m distance (e.g., Figure 8, negative SH polarity corresponds to left first-motion at the source, looking at receiver Array-2). Events with positive SH polarity (right first-motion) exhibit the opposite change in P polarity along the treatment. From this simple relationship, we formed two event groups based on SH polarity and computed composite focal mechanisms constrained by the P-wave polarity data alone (using Reasenber and Oppenheimer's (1985) routine). SH first motions for 90% of the events are to the left, the remaining are to the right. The solutions for both event groups uniquely converged to strike-slip mechanisms consistent with their SH motions and with only 4 to 5% discrepant P-wave first motions (Figure 11). The ratios of the SH- to P-amplitudes (SH/P) for both data groups are consistent with the first-motion-constrained, strike-slip solutions (Figure 12). The same strike-slip solutions were determined for event subsets using a combination of P- and SH-polarities and the amplitude ratios of SH/P-, SV/SH- and SV/P as input to Snoke et al.'s (1984) focal-mechanism routine.

The compositing of the P-wave first-motion data is justified by: 1) the similarity of adjacent-source waveforms throughout the data set (Figure 8); 2) the consistency of both SH first motions and amplitude ratios with the P-polarity-constrained solutions (Figure 12); and 3) the agreement between strike of nodal planes with the event-location trend (Figure 11). The dips of the nodal planes closest to the event trends are poorly constrained by the P-polarities alone (Table 2) due to the limited focal sphere coverage (Figure 11). However, SV amplitudes are generally very low (e.g., Figure 6), and the distribution of SV/SH amplitudes over the treatment length restrict the slip planes to near vertical.

FEATURES AND INTERPRETATION

Focal Mechanisms

As summarized above, the prevalent natural-fracture orientation expected within the reservoir is vertical and striking within 10° of S_{Hmax} . We interpret the focal mechanism groups to represent slip induced on these natural fractures, with the sense of slip determined by the fracture plane's strike relative to S_{Hmax} . The trend of event locations in Figure 10 is N80°E, consistent with independent measurements of S_{Hmax} direction (Laubach and Monson, 1988). Both fault-plane solutions show a nodal plane within 10° of the seismic trend (Figure 11). Although the fault-plane strikes are not statistically distinct (Table 2), they show the correct sense of rotation required to change from left-lateral to right-lateral slip. This relative sense of strike is independently supported by the SH/P amplitude ratios. Mean SH/P ratios for the right-lateral solution (Figure 12, bottom) are shifted about 5° to the right with respect to the left-lateral solution (Figure 12, top), corresponding to a counter-clockwise rotation of the fault-plane strike. Stress heterogeneities along the treatment length could also result in local slip reversal for fractures striking close to S_{Hmax} . However, there is some spatial separation between the two focal mechanism groups that suggest distinct fracture populations. The majority of right-lateral events are along the southern margins of the event trend. There is no temporal distinction; the proportions of the two event groups are fairly constant during pumping and shut-in periods. A predominance of fractures striking slightly clockwise of S_{Hmax} may explain the more frequent occurrence of left-lateral slip.

Depth Distribution of Microseismicity

Figure 13 shows a histogram of the microearthquake depth distribution along with the treatment well's proppant radioactive (RA) tracer log and perforation sub-intervals. Both proppant and fluid were tagged to give a qualitative diagnostic of the treatment behavior near the well. The RA tracer log shows that the propped fracture height was reasonably well contained with the highest concentrations of sand staying close to the perforated depth intervals. We shifted two event subgroups to align the microseismicity with the RA tracer log and perforation intervals; events above 2650 m were shifted down 4 m and events below 2680 m were shifted up 2 m

(Figure 13). The absolute depths of the clusters can be reasonably shifted up or down a few meters, due to velocity uncertainties suggested by the magnitude of station corrections (~1 ms on average). Our shifts to enhance the correlation are also reasonable based on correlations of microseismicity with fracture conductivity and fluid flow at various other sites (e.g., Dreesen et al., 1987; Branagan et al., 1997; Jupe et al., 1998; Rutledge et al., 1998; Tezuka and Niitsuma, 2000; Evans and Jones, 2001).

The containment of seismicity within the target sands suggests that the discrete sand intervals are hydraulically isolated (Figures 10 and 13). This containment is also consistent with activating the reservoir's prevalent natural fractures, which are confined within individual sands and largely absent in the intervening shales (Dutton et al., 1991). Only a few events occur within the top perforation interval (labeled **A** in Figure 13), though the RA tracer log shows high concentrations of proppant near the treatment well. The RA tracer log also detected low-levels of the tagged fluid beneath the Stage-3 perforated section, suggesting channel flow behind casing. Since the seismicity above indicates good intra-perf containment far into formation, we conclude that the banded seismicity below the Stage-3 treatment interval is likely to have resulted from flow behind casing reaching more permeable horizons below.

Treatment Length and Width Development

Figure 14 illustrates the fracture length development during the main portion of the treatment for the two most populous depth clusters. The initial, rapidly attained lengths out to about 150 to 200 m correspond to the lengths developed during the earlier, treated-water injections shown in Figure 4. The space-time event sequences of Figure 14 show envelopes of activity over large lengths of the treatment. Often the envelope edges form clear linear trends, defined by similar magnitude events, suggesting systematic migration of shear dislocations. Although less clear, such linear trends can also be seen within the envelope of active treatment length. The seismicity migrates both away from and towards the treatment well. The positions of individual events oscillates over the envelope length, sometimes jumping from one edge to the other. In general, larger magnitude events occur closer to the treatment well, perhaps simply due to higher pore pressure (Figure 14). As the injection progresses, an aseismic zone develops,

generally expanding away from the treatment well and attaining lengths of about 1/3 to 1/2 of total seismic length. A comparable zone developed during the Stage-2 treatment (see Figure 4c of Urbancic et al., 1999). In both cases the aseismic zone developed soon after injection of the crosslink gel was started. The aseismic zone may be due to the complete relaxation of shear stress and a possible indicator of fracture length being maintained open.

Expanded displays of the best locations (smallest RMS residuals) within these same two depth intervals, show fracture zones widths as narrow as 6 m (Figures 15 and 16). A coarse time sequence illustrated by the symbol type shows a general migration of events normal to the trend for the deeper subcluster, suggesting that the fracture zone widens as the treatment progresses (Figure 15). The widening may be caused by or at least exaggerated by temporal changes in velocities over portions of the travel paths affected by the injection. The shallower subcluster does not show the systematic temporal widening (Figure 16). Instead, late in the treatment, the shallow zone attains about 200 m more length than the deep interval (Figures 16 and 15, respectively, also seen in Figure 10). The event trend also offsets about 6 m to the south at about 230 to 250 m east of the treatment well (Figure 16), possibly caused by a crosscutting structure. The detailed event sequence in length also suggest a breakdown of some barrier associated with the trend offset. Prior to hour 11.5 the event density is high near the fracture terminus at about 230 m (Figure 14, interval C). Following the introduction of proppant flow, seismicity extends eastward at a higher rate (Figure 14) past the trend offset (Figure 16). The proppant may have acted as a fluid diverter, increasing the net pressure over the shallow intervals, by preferentially screening out or impeding flow at the deep perforations.

The general event-sequence patterns, active at once over large lengths of the treatment (Figure 14) and possibly developing width (Figure 15), suggest that multiple, subparallel fractures are being pressurized by leak off (fluid flow and pressure dissipation through the matrix or interconnecting fractures along the treatment length). Studies from numerous other sites indicate that multiple-fracture geometries are commonly created or pressurized during hydraulic fracturing (Mahrer, 1999), including some coring and mineback tests that have revealed total fracture-zone widths and trend-offsets comparable to that resolved in Figures 15 and 16 (e.g., Warpinski and Teufel, 1987; Hopkins et al., 1998).

DISCUSSION

The initial and new event locations indicate treatment geometries very different from predictions. Poor vertical containment and short fracture length was expected based on fairly uniform stress (S_{hmin}) and mechanical-property profiles within the Upper Cotton Valley (McCain et al., 1993; Mayerhofer et al., 2000). Subsequent model calibration allowed a reasonable match with the net pressure data and initial event locations (Mayerhofer et al., 2000). The models treat the fracture growth as a continuous process within the whole perforated section, whereas the new event locations indicate that multiple discrete zones were activated, suggesting that the targeted sands were hydraulically isolated. It is possible that hydraulic fractures propagated through the intervening shales, with the shales deforming aseismically. An interesting analogy to this from natural seismicity may be sections of the San Andreas fault that slide largely aseismically, but are populated by small earthquakes that occur, as in our case, along horizontal bands parallel to the direction of slip (Rubin et al., 1999). Nonetheless, we consider hydraulic isolation to be a reasonable interpretation based on the zones of fluid flow correlating with event locations (Figure 13) and the seismicity's consistency with activating a fracture system that is optimally-oriented for flow and already contained within the target sand intervals.

Patterns of S- to P-wave energy ratios (E_s/E_p) were previously interpreted as an indicator of a non-shear or volumetric component of failure that varies systematically along the Cotton Valley treatment lengths (Urbancic and Zinno, 1998; Rutledge and Urbancic, 1999; Mayerhofer et al., 2000). The same data, displayed as amplitude ratios in Figure 12, can instead be attributed to the radiation patterns of two similar, double-couple, shear mechanisms occurring uniformly over the treatment length. The P- and SH-polarity changes, waveform similarity, new locations and natural fracture geometry all support our interpretation of uniform failure mechanisms. Further, for a treatment in well 21-09 at the same depth (Figure 2), we found identical patterns of polarities and amplitude ratios with respect to the common monitor well (Array-2, see Figure 3 of Rutledge and Phillips, 2002). Assuming a Coulomb failure criteria, our observations of horizontal slip along fractures subparallel to S_{Hmax} imply a relatively high critical pore pressure. The uniformity of this source mechanism thereby implies a lack of natural fractures more favorably oriented for shear failure (fractures with higher resolved shear stress, lower critical pore pressure).

Pressurizing the existing fractures may be the primary process of enhancing permeability and fracture network conductivity over most of the length attained, rather than creating fresh hydraulic fractures. The high pore pressure required for shear slip should be approaching fracture opening pressures. Hence, incremental pressure increases are likely to extend the shear-active fractures as hydraulic fractures, improving the chances of connecting subparallel fracture strands. Although seismically we primarily observe shear slip, the patterns of event sequences in Figure 14 are consistent with extending existing fractures, with the shear events being the precursors to opening and incremental growth. Shear stress transferred by the strike-slip displacements would load the fracture zone ahead and behind the rupture perimeters. This would further promote strike-slip failure, resulting in the repetitive, linear migrations. If the trailing aseismic zone represents the fracture length being maintained open, as pressure further increases, then it may in turn indicate the lengths over which proppant would most easily be carried into the formation.

High critical pore pressure also implies slip occurs at low effective normal stresses, which favors permeability creation through shear dilation. In general, slip occurring under lower normal stress will allow higher dilation angle and reduce the shearing-off of steeper, short-wavelength asperities, resulting in more effective, permanent dilation than shearing under higher normal stress (see Evans et al., (1999) and references therein). Conditions favoring effective shear dilation further supports the self-propping mechanisms suggested by other investigators for the success of Cotton Valley treatments using water and very low proppant concentrations (Mayerhofer et al., 1997; Mayerhofer and Meehan, 1998).

Why Strike-Slip Faulting?

The prevalence of strike-slip faulting is surprising. Using Zoback and Healy's (1984) criteria, effective stress ratio of overburden (S_V) and S_{hmin} at hydrostatic pore pressure implies a critically stressed condition for normal faulting at reservoir depths. Local neotectonic activity has occurred primarily as normal faulting (Collins et al., 1980; Pennington and Carlson, 1984). It is therefore unlikely that S_{Hmax} exceeds S_V . Since the natural fractures show both dip and strike angles subparallel to S_V and S_{Hmax} , respectively, the propensity for dip-slip motion should be greater or comparable to the propensity for strike-slip motion. Dutton et al. (1991) noted that

fracture curvature commonly results in opposed dip directions along vertical fracture traces within the Cotton Valley formation; this could inhibit vertical slip. As an alternative or additional mechanism to inhibit vertical slip, we speculate that for planar, near-vertical fractures through horizontal beds, the shear strength across the rock fabric (dip-slip direction) may be significantly greater than along the lamination direction (strike-slip direction). Finally, elevating the pore pressure throughout the cylindrical rock volumes, inferred from the horizontal microearthquake clusters, will result in the poroelastic effect of increasing stress primarily along the volume's major axis (S_{Hmax} direction), thus promoting strike-slip faulting along the treatment length (e.g., Segall and Fitzgerald, 1998).

CONCLUSIONS

We have re-located the microearthquake events for an Upper Cotton Valley hydraulic fracture stimulation using high-precision arrival-time data obtained from the waveforms. Compared to the original locations, the new arrival-time data result in 4-fold improvement in location precision. The new locations are vertically contained within the individual, targeted sands, suggesting little or no hydraulic communication between discrete perforation intervals over an 80-m stimulated section. Treatment lengths at the shallow perforation intervals are about 200 m greater than at the deeper intervals. The event-sequence patterns suggest that the length differences may be due to proppant preferentially impeding flow at the deeper intervals. The highest quality locations indicate that fracture zone widths were as narrow as 6 m. Seismicity that occurred below the injection depths is likely to have resulted from fluid flow behind casing and then out into permeable horizons below.

The similarity of waveforms from nearby events seen throughout the data set, along with systematic changes of phase amplitude ratios and first-motion polarities, indicate two fairly uniform focal mechanisms occurring over the entire fracture length. Composite focal mechanisms indicate both left- and right-lateral strike-slip faulting along near-vertical fractures that strike subparallel to S_{Hmax} .

The focal mechanisms and event locations are consistent with activation of the reservoir's

known natural fracture system, a system that is dominated by vertical fractures isolated within individual sands and that trend subparallel to expected the hydraulic fracture orientation. Activation of these fractures indicates a stronger correlation of seismicity with low-impedance flow paths than is normally found during injection stimulation. Since the seismically-active fractures are not optimally oriented for shear slip, critical pore pressures should be high, probably approaching crack-opening pressures. Incremental pore-pressure increases are likely to subsequently extend the shear-active fractures as hydraulic fractures, improving the chances of connecting multiple, subparallel fracture strands. High critical pore pressure also implies low effective-normal-stress conditions for slip, a condition that should favor more effective permeability creation via shear dilation.

ACKNOWLEDGEMENTS

Robert Withers and Robert Dart acquired and compiled the microseismic data for The Cotton Valley Hydraulic Fracture Imaging Project. All other information and data generated by the Project were compiled and archived by Branagan & Associates. Many people have contributed discussions, ideas and/or information that were helpful to the work presented: We thank Leigh House, Mike Fehler, Norm Warpinski, Mike Mayerhofer, Ted Urbancic, Don Brown, Keith Evans, Rob Jones, Jim Albright, Rich Peterson and Buddy Woodroof. The Cotton Valley Imaging Consortia supported the initial mapping efforts from which this work was started. We are especially thankful to Dick Zinno, Ray Walker, Steve Wolhart and John Gibson for encouraging our participation in the Project. Thanks also to Ken Mahrer and two anonymous reviewers for suggestions to improve the manuscript. This work was funded by the U.S. Department of Energy's National Petroleum Technology Office and the Gas Technology Institute.

REFERENCES

- Aki, K. and Richards, P.G., 1980, Quantitative seismology, theory and methods: W.H. Freeman and Co., San Francisco.
- Albright, J.N., and Pearson, C.F., 1982, Acoustic emissions as a tool for hydraulic fracture location: Experience at the Fenton Hill Hot Dry Rock site: Soc. Petro. Eng. J., August, 523-530.

- Branagan, P.T., Peterson, R.E., Warpinski, N.R., Wolhart, S.L., and Hill, R.E., 1997, Propagation of a hydraulic fracture into a remote observation wellbore: Results of C-Sand experimentation at the GRI/DOE M-Site Project: Paper 38574, Proc. 1997 Soc. Petro. Eng., Ann. Tech. Conf., San Antonio, Texas.
- Brown, S.R., and Bruhn, R.L., 1998, Fluid permeability of deformable fracture networks: J. Geophys. Res., **103**, 2489-2500.
- Collins, E.W., Hobday, D.K., and Kreitler, C.W., 1980, Quaternary faulting in East Texas: Univ. Texas Austin, Bureau Econ. Geol. Circular 80-1, 20 p.
- Cornet, F.H. and Yin, J., 1995, Analysis of induced seismicity for stress field determination and pore pressure mapping: Pure Appl. Geophys., **145**, 677-700.
- Cornet, F.H., 2000, Comment on 'Large-scale in situ permeability tensor of rocks from induced microseismicity' by S.A. Shapiro, P. Audigane and J.-J. Royer: Geophys. J. Int., **140**, 465-469.
- Dreesen, D.S., Malzahn, M.V., Fehler, M.C., and Dash, Z.V., 1987, Identification of MHF fracture planes and flow paths: A correlation of well log data with patterns in locations of induced seismicity: Trans. Geotherm. Res. Council., 339-343.
- Dutton, S.P., Laubach, S.E., Tye, R.S., and Diggs, T.N., 1991, Geological analysis of the Travis Peak formation and Cotton Valley sandstone: *in* Staged Field Experiment No. 3: Application of advanced technologies in tight gas sandstones - Travis Peak and Cotton Valley Formations, Waskom Field, Harrison County, Texas, (Eds.) CER Corp. and S.A. Holditch Assoc., Inc., Gas Research Instit., Report No. GRI-91/0048.
- Evans, K.F., Cornet, F.H., Hashida, T., Hayashi, K., Ito, T., Matsuki, K., and Wallroth, T., 1999, Stress and rock mechanics issues of relevance to HDR/HWR engineered geothermal systems: Review of developments during the past 15 years: Geothermics, **28**, 455-474.
- Evans, K.F., and Jones, R.H., 2001, Hydrologically-significant structures imaged by induced microseismicity in a 3-km deep well in granite at Soultz: Euro. Assoc. Geosci. Eng. / Soc. Explor. Geophys., Research Workshop on Reservoir Rocks, Expanded Abstracts, Pau, France.
- Fehler, M.C., 1989, Stress control of seismicity patterns observed during hydraulic fracturing experiments at the Fenton Hill Hot Dry Rock geothermal site, New Mexico: Int. J. Rock Mech. Min Sci & Geomech. Abstr., **26**, 211-219.

- Fehler, M., Jupe, A., and Asanuma, H., 2001, More Than Cloud: New Techniques for characterizing reservoir structures using induced seismicity: *The Leading Edge*, **20**, 324-328.
- Flinn, E.A., 1965. Signal analysis using rectilinearity and direction of particle motion. *Proc. I.E.E.E.*, **53**, 1725-1743.
- Frohlich, C., 1979, An efficient method for joint hypocenter determination for large groups of earthquakes: *Comput. Geosci.*, **5**, 387-389.
- Gaucher, E., Cornet, F.H., and Bernard, P., 1998, Induced seismicity analysis for structure identification and stress field determination: Paper 47324, *Proc. 1998 Soc. Petro. Eng. / Int. Soc. Rock Mech., Eurock '98 Conf., Trondheim, Norway*.
- Hopkins, C.W., Rosen, R.L., and Hill, D.G., 1998, Characterization of an induced hydraulic fracture completion in a naturally fractured Antrim shale reservoir: Paper 51068, *Proc. 1998 Soc. Petro. Eng. Eastern Regional Mtg., Pittsburgh, Pennsylvania*.
- House, L., 1987, Locating microearthquakes induced by hydraulic fracturing in crystalline rock: *Geophys. Res. Lett.*, **14**, 919-921.
- Jones, R.H., Beauce, A., Jupe, A., Fabriol, H., and Dyer, B.C., 1995, Imaging induced microseismicity during the 1993 injection test at Soultz-sous-Forêts, France: *Proc. World Geotherm. Cong., Florence*, 2665-2669.
- Jones, R.H., and Stewart, R.C., 1997, A method for determining significant structures in a cloud of earthquakes: *J. Geophys. Res.*, **102**, 8245-8254.
- Jupe, A., Jones, R., Dyer, B., and Wilson, S., 1998, Monitoring and management of fractured reservoirs using induced microearthquakes activity: Paper 47315, *Proc. 1998 Soc. Petro. Eng. / Int. Soc. Rock Mech., Eurock '98 Conf., Trondheim, Norway*.
- Laubach, S.E., 1988, Subsurface fractures and their relationship to stress history in East Texas basin sandstone: *Tectonophysics*, **156**, 37-49.
- Laubach, S.E., and Monson, E.R., 1988, Coring-induced fractures: Indicators of hydraulic fracture propagation in a naturally fractured reservoir: Paper 18164, *Proc. 1988 Soc. Petro. Eng., Ann. Tech. Conf., Houston, Texas*.
- McCain, W.D., Voneiff, G.W., Hunt, E.R., and Semmelbeck, M.E., 1993, A tight gas field study: Carthage (Cotton Valley) field: Paper 26141, *Proc. 1993 Soc. Petro. Eng. Gas Tech. Symp.*,

Calgary, Canada.

- Mahrer, K.D., 1999, A review and perspective on far-field hydraulic fracture geometry studies: J. Petro. Sci. Eng., **24**, 13-28.
- Mayerhofer, M.J., and Meehan, D.N., 1998, Waterfracs - Results from 50 Cotton Valley Wells: Paper 49104, Proc. 1998 Soc. Petro. Eng., Ann. Tech. Conf., New Orleans, Louisiana.
- Mayerhofer, M.J., Richardson, M.F., Walker, Jr., R.N., Meehan, D.N., Oehler, M.W., and Browning, Jr., R.R., 1997, Proppants? We don't need no proppants: Paper 38611, Proc. 1997 Soc. Petro. Eng., Ann. Tech. Conf., San Antonio, Texas.
- Mayerhofer, M.J., Walker, Jr., R.N., Urbancic, T., and Rutledge, J.T., 2000, East Texas Hydraulic Fracture Imaging Project: Measuring hydraulic fracture growth of conventional sandfracs and waterfracs: Paper 63034, Proc. 2000 Soc. Petro. Eng., Ann. Tech. Conf., Dallas, Texas.
- Moriya, H., Nagano, K., and Niitsuma, H., 1994, Precise source location of AE doublets by spectral matrix analysis of triaxial hodogram: Geophysics, **59**, 36-45.
- Moriya, H., Nakazato, K., Niitsuma, H., and Baria, R., 2002, Detailed fracture system of the Soultz-sous-Forêts HDR field evaluated using microseismic multiplet analysis: Pure Appl. Geophys., **159**, 517-541.
- Pearson, C., 1981, The relationship between microseismicity and high pore pressures during hydraulic stimulation experiments in low permeability granitic rocks: J. Geophys. Res., **86**, 7855-7864.
- Pennington, W.D., and Carlson, S.M., 1984, Observations from the East Texas seismic network (June 1981-August 1982): Univ. Texas Austin, Bureau Econ. Geol. Circular 84-3, 48 p.
- Phillips, W.S., House L.S., and Fehler, M.C., 1997, Detailed joint structure in a geothermal reservoir from studies of induced microearthquake clusters: J. Geophys. Res., **102**, 11745-11763.
- Phillips, W.S., Fairbanks, T.D., Rutledge, J.T., and Anderson, D.W., 1998, Induced microearthquake patterns and oil-producing fracture systems in the Austin Chalk: Tectonophysics, **289**, 153-169.
- Phillips, W.S., 2000, Precise microearthquake locations and fluid flow in the geothermal reservoir at Soultz-sous-Forêts, France: Bull Seism. Soc. Am., **90**, 212-228.

- Reasenber, P. and Oppenheimer, D., 1985, FPFIT, FPLOT and FPPAGE: Fortran computer programs for calculating and displaying earthquake fault-plane solutions: U.S. Geological Survey, Open-File Report 85-0739.
- Roff, A., Phillips, W.S. and Brown, D.W., 1996. Joint structures determined by clustering microearthquakes using waveform amplitude ratios: *Int. J. Rock Mech. and Min. Sci. and Geomech. Abstr.*, **33**, 627-639.
- Rowe, C.A., Aster, R.C., Phillips, W.S., Jones, R.H., Borchers, B., and Fehler, M.C., 2002, Using automated, high-precision repicking to improve delineation of microseismic structures at the Soultz geothermal reservoir: *Pure Appl. Geophys.*, **159**, 563-596.
- Rubin, A.M., Gillard, D., and Got, J.L., 1999, Streaks of microearthquakes along creeping faults: *Nature*, **400**, 635-641.
- Rutledge, J., 1998, Analyses of the Cotton Valley microseismic data for asymmetric fracture growth: *in* Cotton Valley Hydraulic Fracture Imaging and Waterfrac Projects, Data and Information Archive, Project Phases I, II, III and IV, Gas Research Instit., Report No. GRI-99/0269.
- Rutledge, J.T., Phillips, W.S., and Schuessler, B.K., 1998, Reservoir characterization using oil-production-induced microseismicity, Clinton County, Kentucky: *Tectonophysics*, **289**, 129-152.
- Rutledge, J., and Urbancic, T., 1999, Cotton Valley Imaging Project, Phase IV, Completion of microseismic mapping of the Phase I and II hydraulic fractures, wells CGU21-10 and CGU21-09: *in* Cotton Valley Hydraulic Fracture Imaging and Waterfrac Projects, Data and Information Archive, Project Phases I, II, III and IV, Gas Research Instit., Report No. GRI-99/0269.
- Rutledge, J.T., and Phillips, W.S., 2002, A comparison of microseismicity induced by gel-proppant- and water-injected hydraulic fractures, Carthage Cotton Valley gas field, East Texas: 72nd Ann. Mtg., Soc. Explor. Geophys., Expanded Abstracts.
- Segall, P. and Fitzgerald, S.D., 1998, A note on induced stress changes in hydrocarbon and geothermal reservoirs: *Tectonophysics*, **289**, 117-128.
- Sneddon, I.N., 1946, The distribution of stress in the neighborhood of a crack in an elastic solid: *Proc. Roy. Soc.*, **187**, 229-260.

- Snoke, J.A., Munsey, J.W., Eague, A.G., and Bollinger, G.A., 1984, A program for focal mechanism determination by combined use of polarity and SV-P amplitude ratio data: *Earthquake Notes*, **55**, p. 15.
- Tezuka, K., and Niitsuma, H., 2000, Stress estimated using microseismic clusters and its relationship to fracture systems of the Hijiori hot dry rock reservoir: *Eng. Geology*, **56**, 47-64.
- Urbancic, T.I., and Zinno, R.J., 1998, Cotton Valley Hydraulic Fracture Imaging Project: Feasibility of determining fracture behavior using microseismic event locations and source parameters: 68th Ann. Mtg., Soc. Explor. Geophys., Expanded Abstracts, 964-967.
- Urbancic, T.I., Shumila, V., Rutledge, J.T., and Zinno, R.J., 1999, Determining hydraulic fracture behavior using microseismicity: Proc. 37th U.S. Rock Mech. Symp., 991-997, Vail, Colorado.
- Urbancic, T.I., and Rutledge, J., 2000, Using microseismicity to map Cotton Valley hydraulic fractures: 70th Ann. Mtg., Soc. Explor. Geophys., Expanded Abstracts, 1444-1448.
- Vaidyanathan, P.P., 1990, Multirate digital filters, filter banks, polyphase networks, and applications: A tutorial: Proc. I.E.E.E., **78**, 56-93.
- Walker, Jr., R.N., 1997, Cotton Valley Hydraulic Fracture Imaging Project: Paper 38577, Proc. 1997 Soc. Petro. Eng., Ann. Tech. Conf., San Antonio, Texas.
- Warpinski, N.R., and Teufel, L.W., 1987, Influence of geologic discontinuities on hydraulic fracture propagation: *J. Petro. Tech.*, February, 209-220.
- Warpinski, N.R., Engler, B.P., Young, C.J., Peterson, R.E., Branagan, P.T., Fix, J.E., 1995, Microseismic mapping of hydraulic fractures using multi-level wireline receivers: Paper 30507, Proc. 1995 Soc. Petro. Eng., Ann. Tech. Conf., Dallas, Texas.
- Withers, R.J. and Dart, R.P., 1997, Cotton Valley Production Stimulation Hydrofracture Microseismic Monitoring & Imaging, Data Collection and Analysis Report: *in* Cotton Valley Hydraulic Fracture Imaging and Waterfrac Projects, Data and Information Archive, Project Phases I, II, III and IV, Gas Research Instit., Report No. GRI-99/0269.
- Zoback, M.D., and Healy, J.H., 1984, Friction, faulting and in situ stress: *Annales Geophysicae*, **2**, 689-698.

Hydraulic Stimulation of Natural Fractures

Station	Original Locations		High-Precision Locations	
	P	S	P	S
2-38	0.8	1.0	0.2	0.2
2-33	0.8	0.9	0.2	0.2
2-30	0.9	1.3	0.2	0.2
2-24	1.0	0.9	0.3	0.3
2-20	1.0	0.7	0.3	0.2
2-12	1.4	0.8	*	0.1
2-08	1.2	0.9	*	0.2
2-04	2.8	1.0	*	0.3
1-34	*	1.3	*	0.2
1-19	*	0.9	*	0.8

Table 1: Standard deviation of traveltimes residuals (ms) for the original locations (Figure 9) and the high-precision pick locations (Figure 10). Station locations are shown in Figure 3. The * symbols indicate data not used or not obtained.

Composite Solutions	Observations	Discrepant First Motions	Strike	Dip	Rake
Left Lateral	1000	49	N80°E ±10°	85° ±40°	0° ±10°
Right Lateral	307	12	N70°E ±3°	80° ±40°	180° ±10°

Table 2: Summary of P-wave fault plane solutions shown in Figure 11 with uncertainties for the nodal planes nearest to the event-location trend. Rake of 0° = left lateral displacement, 90° = reverse (thrust), ±180° = right lateral, -90° = normal.

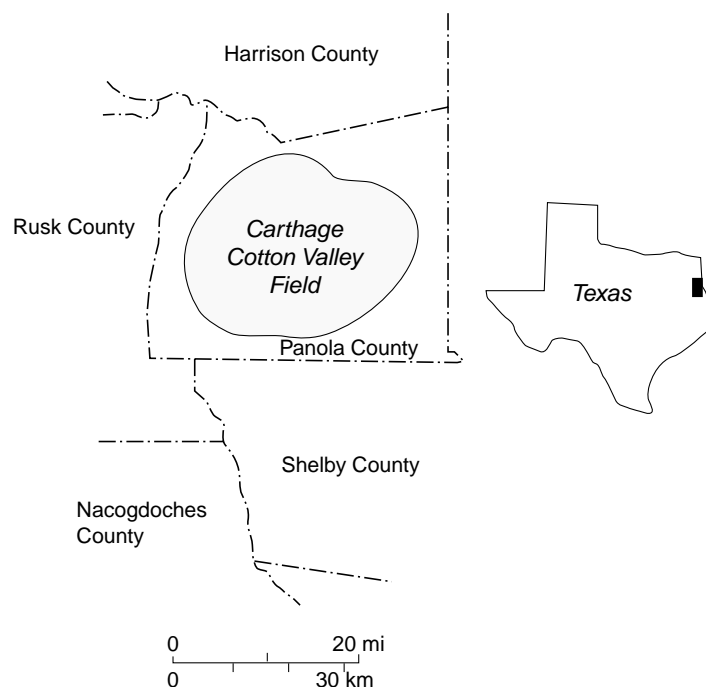


Fig. 1. Location of Carthage Cotton Valley gas field.

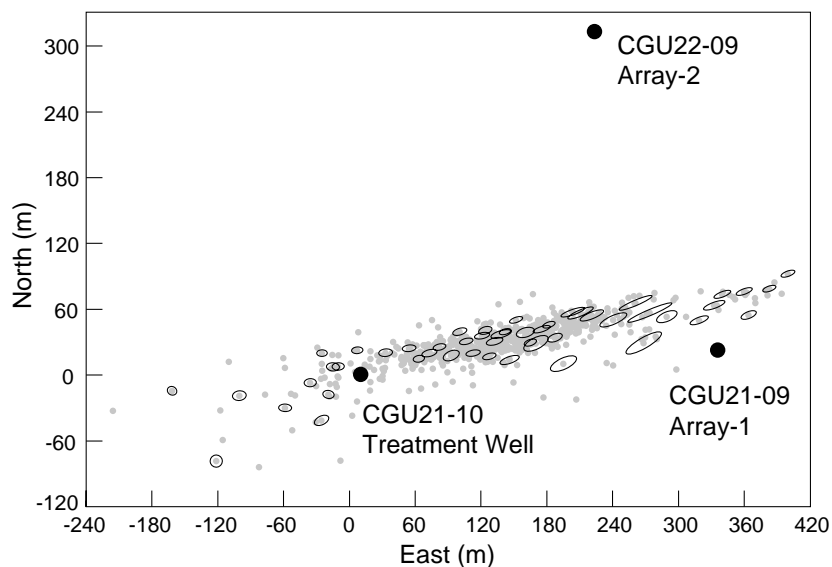


Fig. 2. Treatment and monitor wells and the initial Stage-3 event locations. Some representative error ellipsoid projections are also shown. Datum for all maps herein is the Kelly bushing of CGU21-10 at 119 m above sea level.

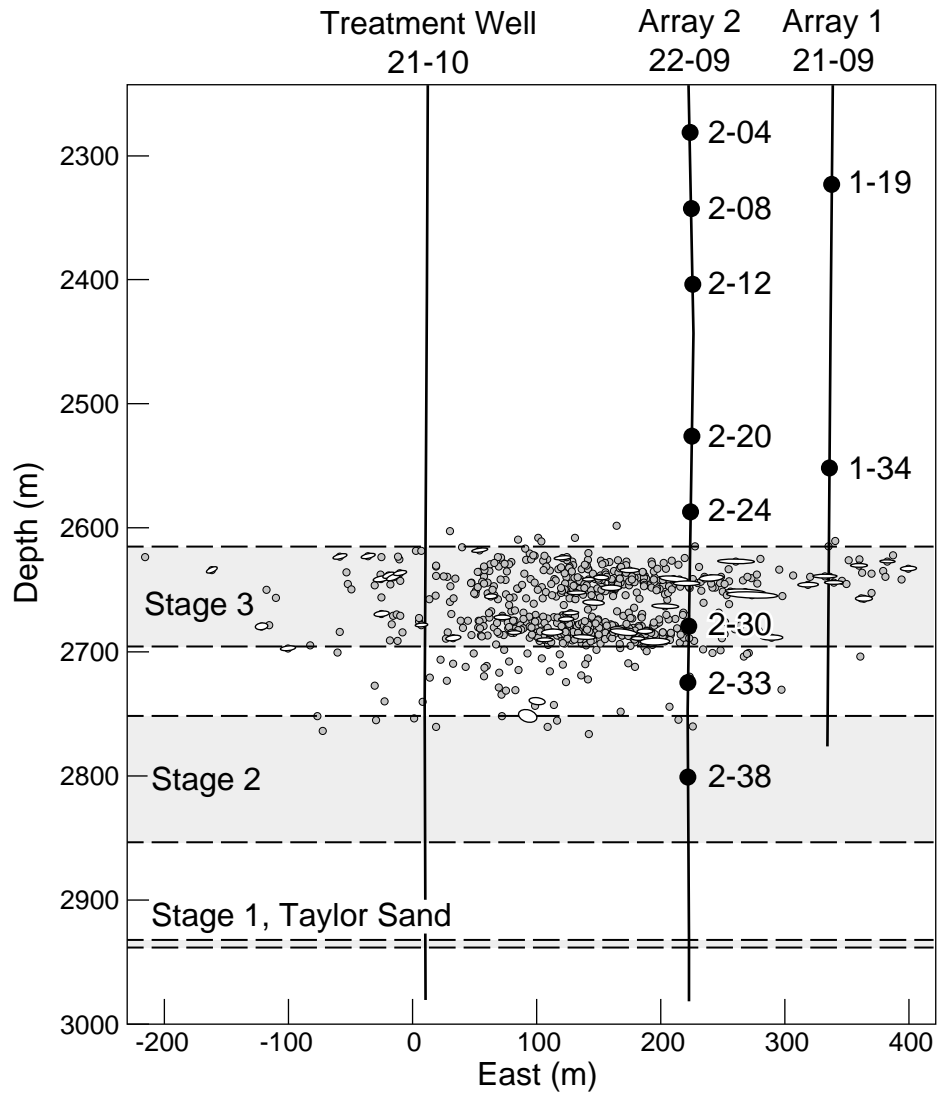


Fig. 3. Depth view of treatment and monitor wells. Three hydraulic fracture completions stages were conducted in the treatment well 21-10. The Stage-3 event locations are shown (same as Figure 2) along with the geophone stations used for determining the locations. Representative error ellipsoid projections are shown.

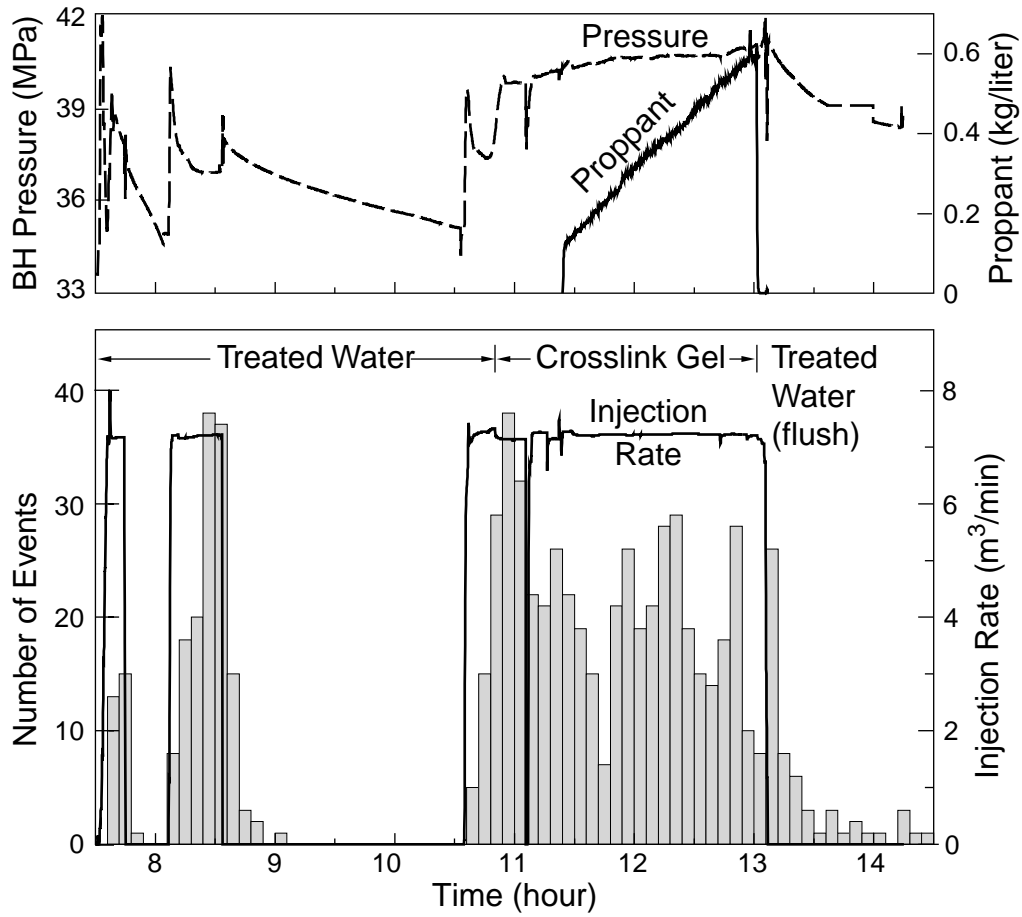


Fig. 4. The Stage-3 hydraulic fracture treatment data and histogram of the induced microseismic events. BH Pressure is the measured bottom-hole pressure.

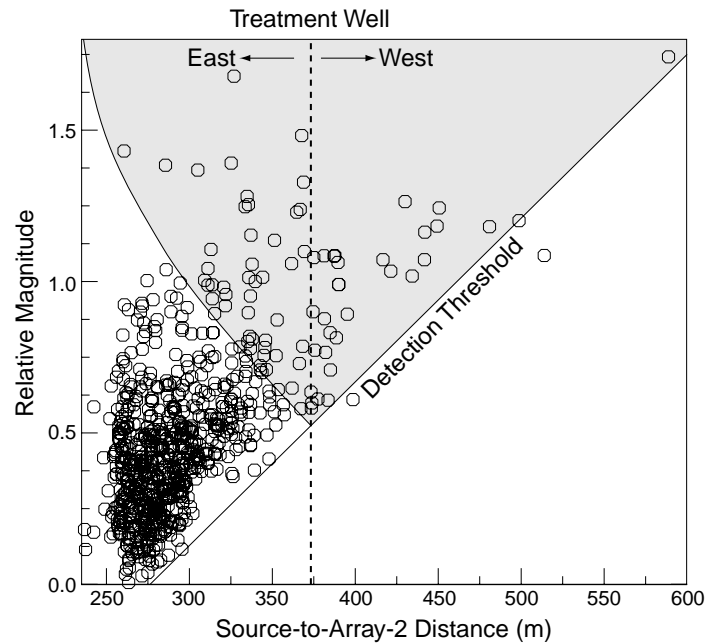


Fig. 5. Relative event magnitudes versus source-receiver distance. The sloping line represents the approximate event detection threshold at Array-2; most events falling below the line would not be detected with signal strength sufficient to be located. The vertical dashed line is at the horizontal distance between the Array-2 well and the treatment well. The curve extending up to the left was determined by obtaining detection thresholds from the sloping line for distances between Array-2 and trial source locations incremented along the western trend of the treatment. These magnitude thresholds were then plotted versus the distance between Array-2 and the symmetric source location, flipped 180° (eastward) about the treatment well.

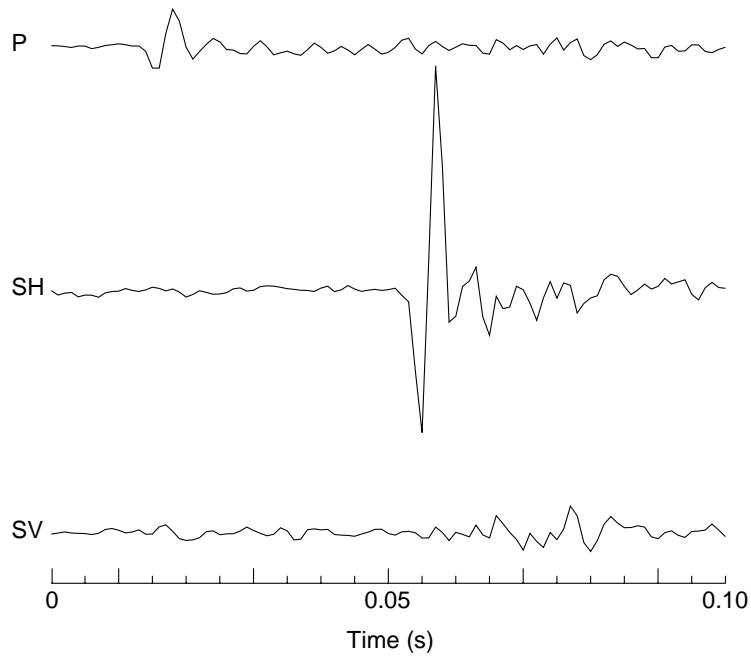


Fig. 6. An example of a typical high-quality microearthquake waveform recorded on station 2-24 that has been rotated into P, SH and SV components. All traces are plotted at the same relative amplitude scale.

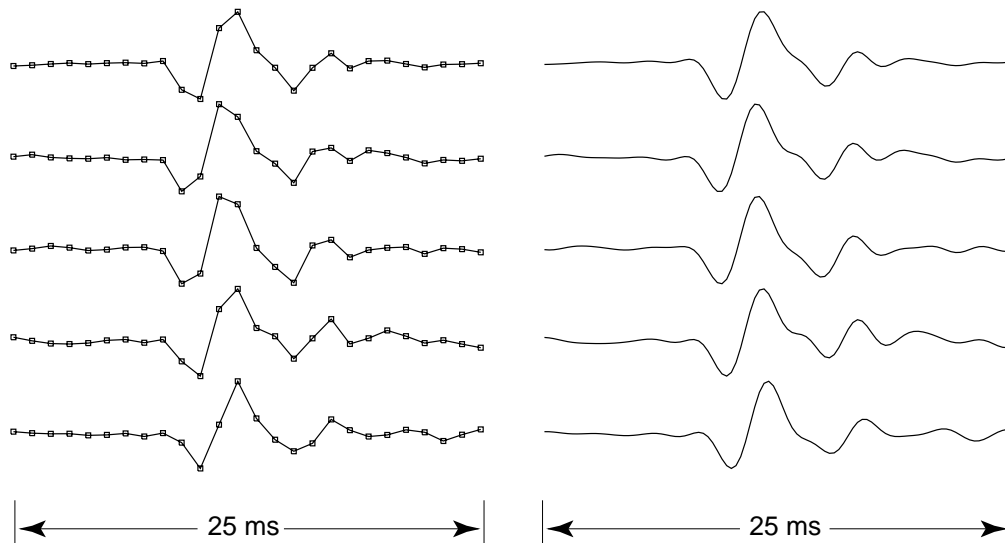


Fig. 7. An example of five similar P-waves from station 2-38. The original data sampled at a 1-ms sample interval (left), and the same waveforms after upsampling 5-fold by spectral interpolation using a FIR filter (right). Each trace is scaled to its maximum amplitude.

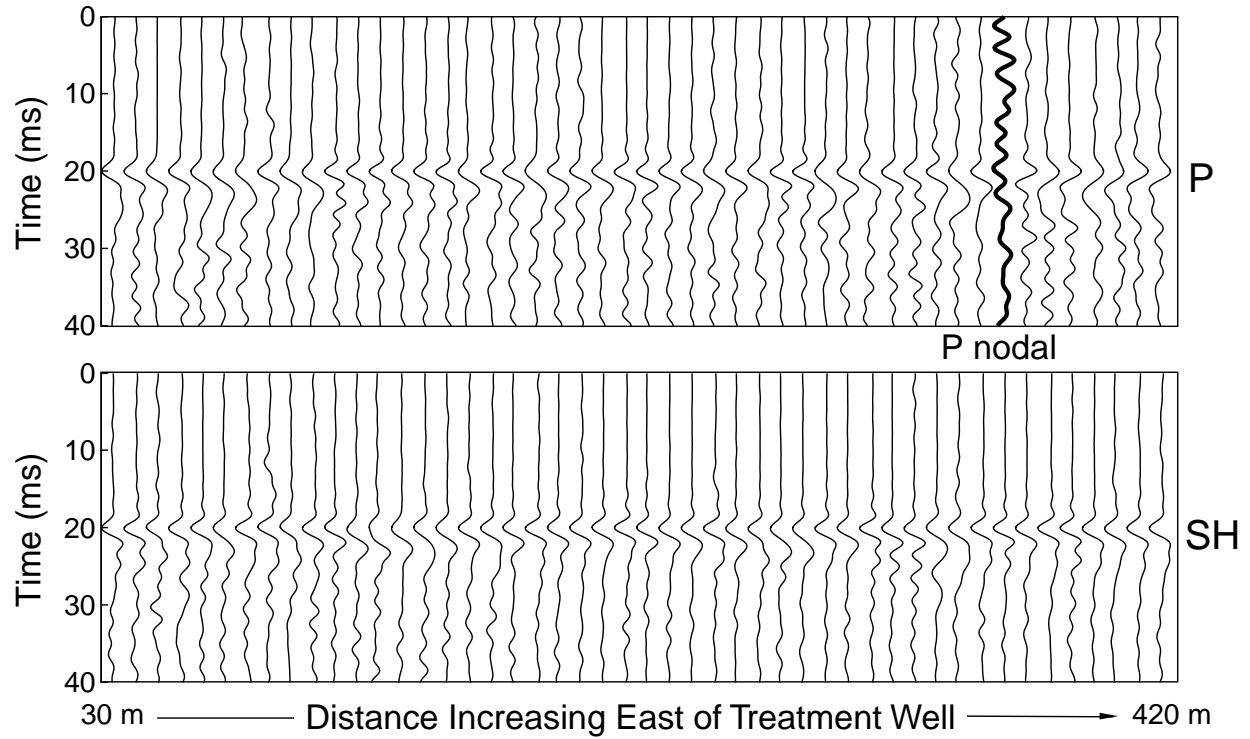


Fig. 8. P and SH waveforms for 50 high-quality (larger magnitudes) microearthquakes with left SH first motions. The waveforms are sorted by event locations, west to east, spaced at a mean horizontal distance of 8 m. The corresponding locations are not evenly spaced. The P-nodal trace (bold) is from an event located 263 m east of the treatment well. P arrivals are from station 2-33 and SH arrivals are from station 2-38 (Figure 3). Each trace is scaled to its maximum amplitude and is windowed to align the arrival-time pick at 20 ms.

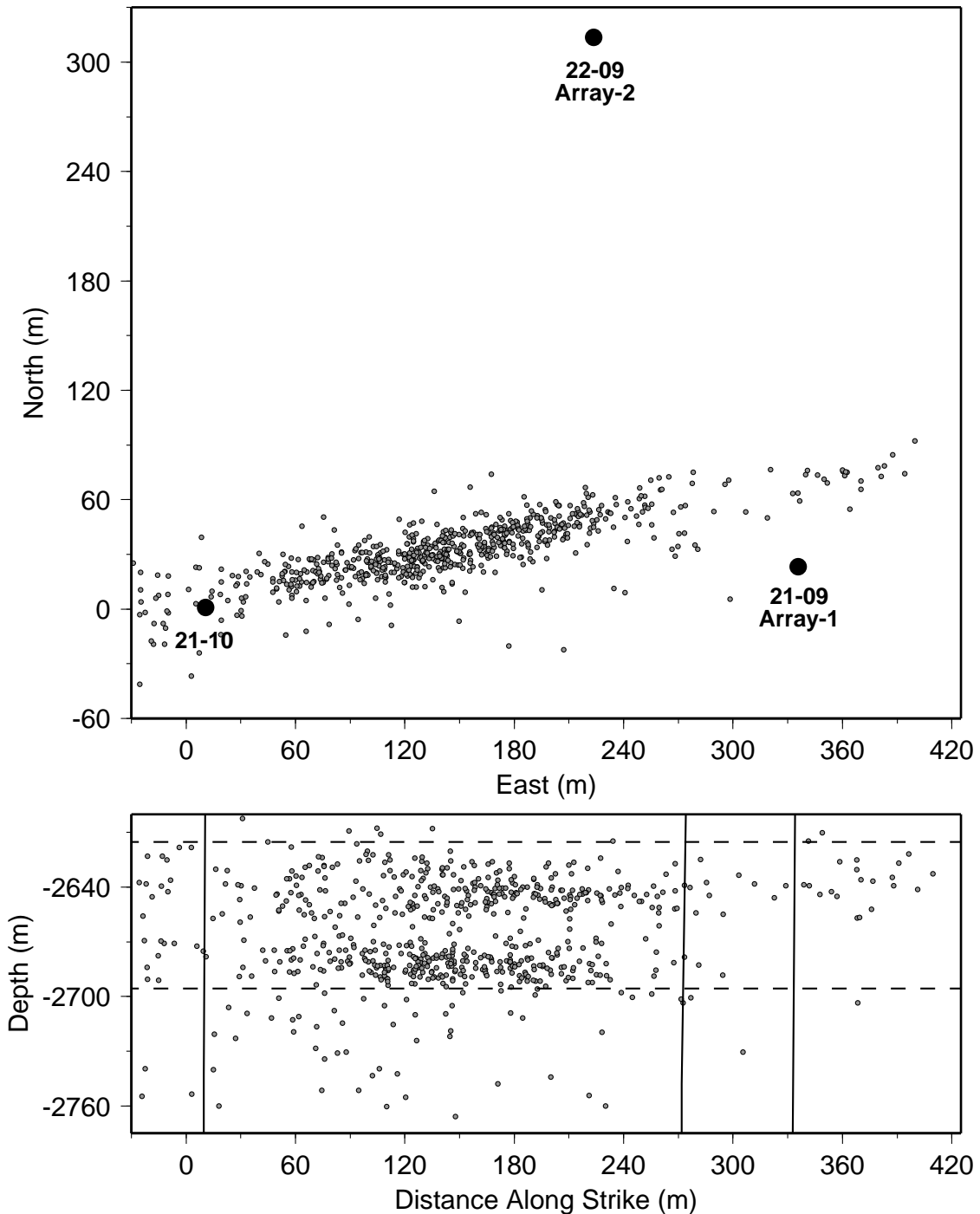


Fig. 9. Original Stage-3 microearthquake locations. Same locations as Figures 2 and 3, but only the events near and east of the treatment well are displayed. The dashed lines mark the Stage-3 injection interval. The vertical lines mark the depth projections of the treatment and monitor wells.

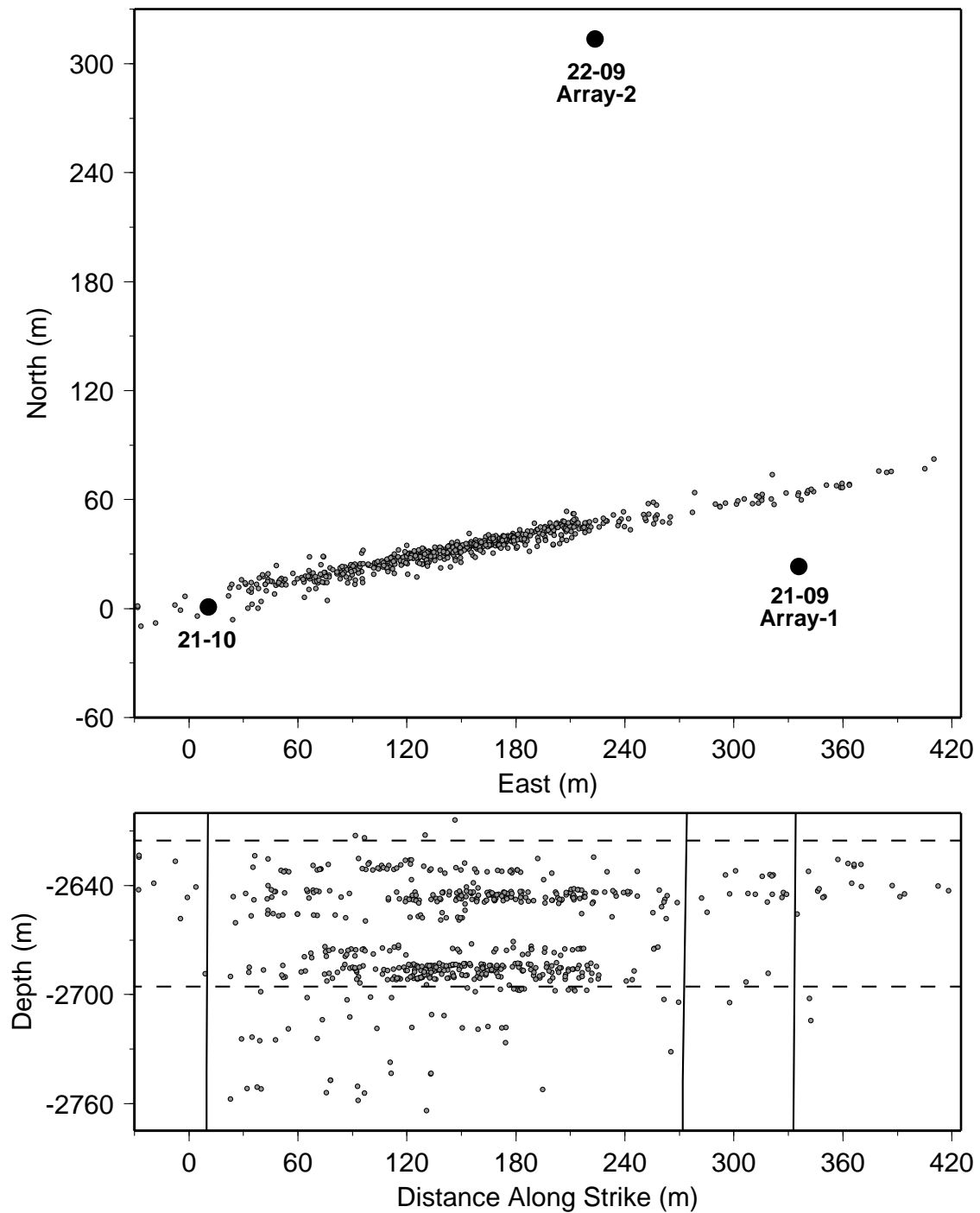


Fig. 10. Same as Figure 9 after obtaining higher-precision arrival-time data.

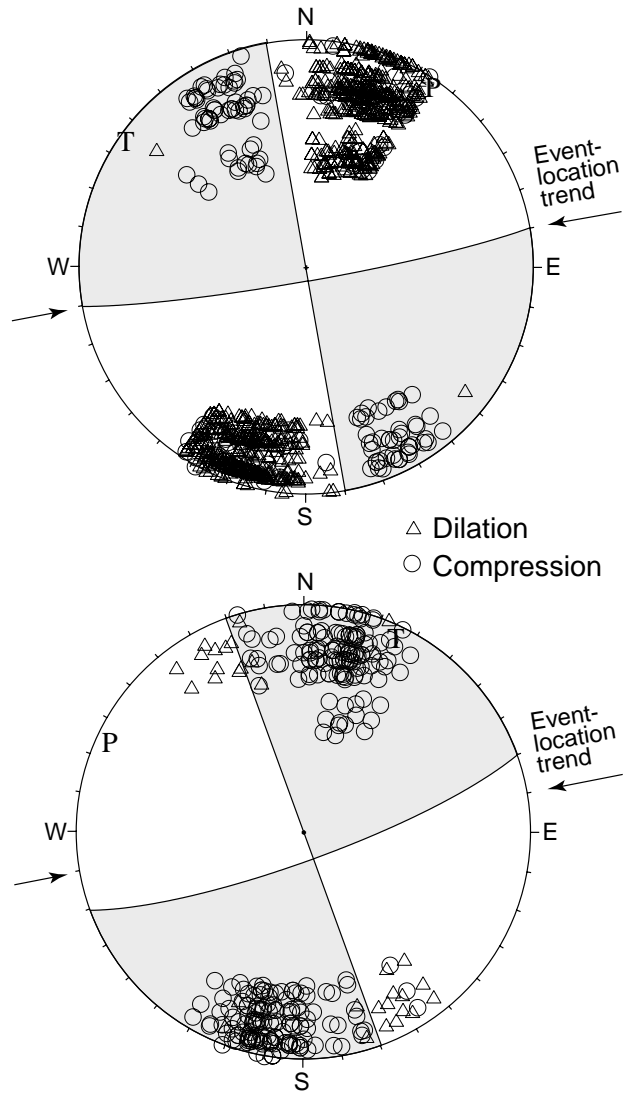


Fig. 11. Composite focal mechanisms using the P-wave first-motion data from all eight stations of Array-2. The compressive quadrants are shaded. The solution for the events with SH first motions to the left is at the top; the lower solution is for events with SH first motions to the right. Input to the focal-mechanism routine was limited to 1000 P-wave first motions. A data-use criteria based on signal-to-noise ratios results in the data gap spanning the nodal plane trending close to N-S (top). All data for the smaller, second group were used (307 first motions, bottom).

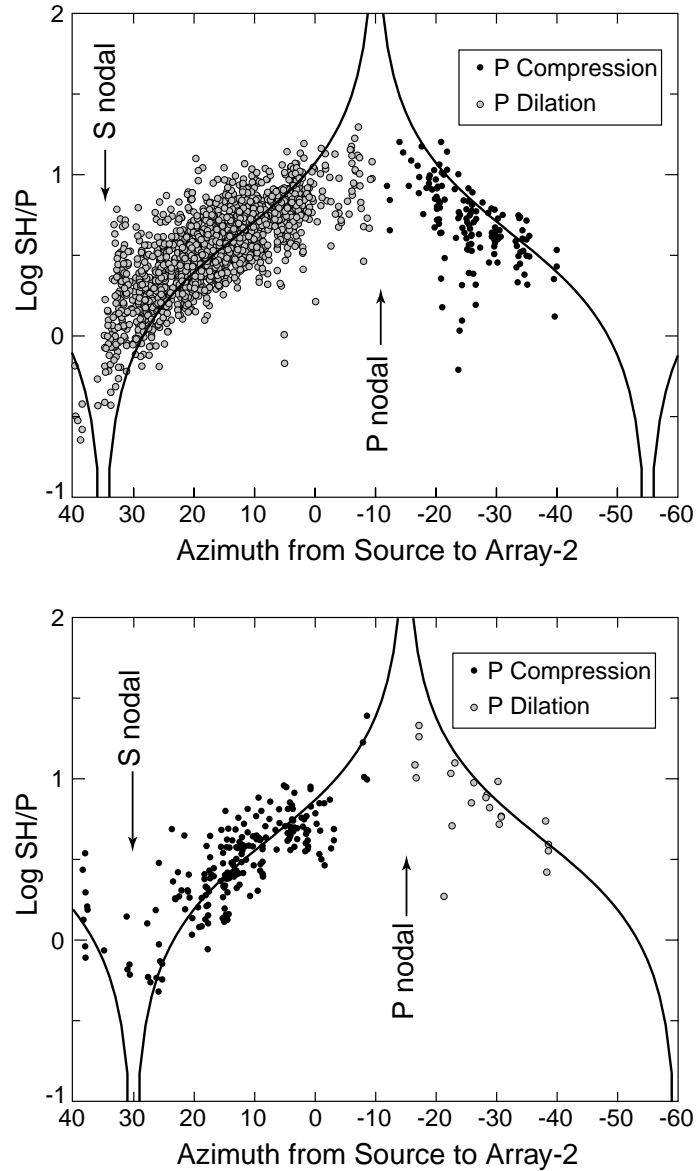


Fig. 12. SH/P amplitude ratios as a function of azimuth from event to station. The plots correspond to the top and bottom focal mechanisms of Figure 11. Data are from the 5 lower stations of Array-2 (Figure 3). All data with P and SH polarities consistent with the focal mechanisms of Figure 11 are shown (95% of all events). The curves are the theoretical SH/P amplitude ratios for a vertical, strike-slip fault striking N80°E (top) and N75°E (bottom) at horizontal take-off angle (Aki and Richards, 1980). P-polarities are also distinguished. The treatment well is near the SH-nodal azimuth with respect to Array-2.

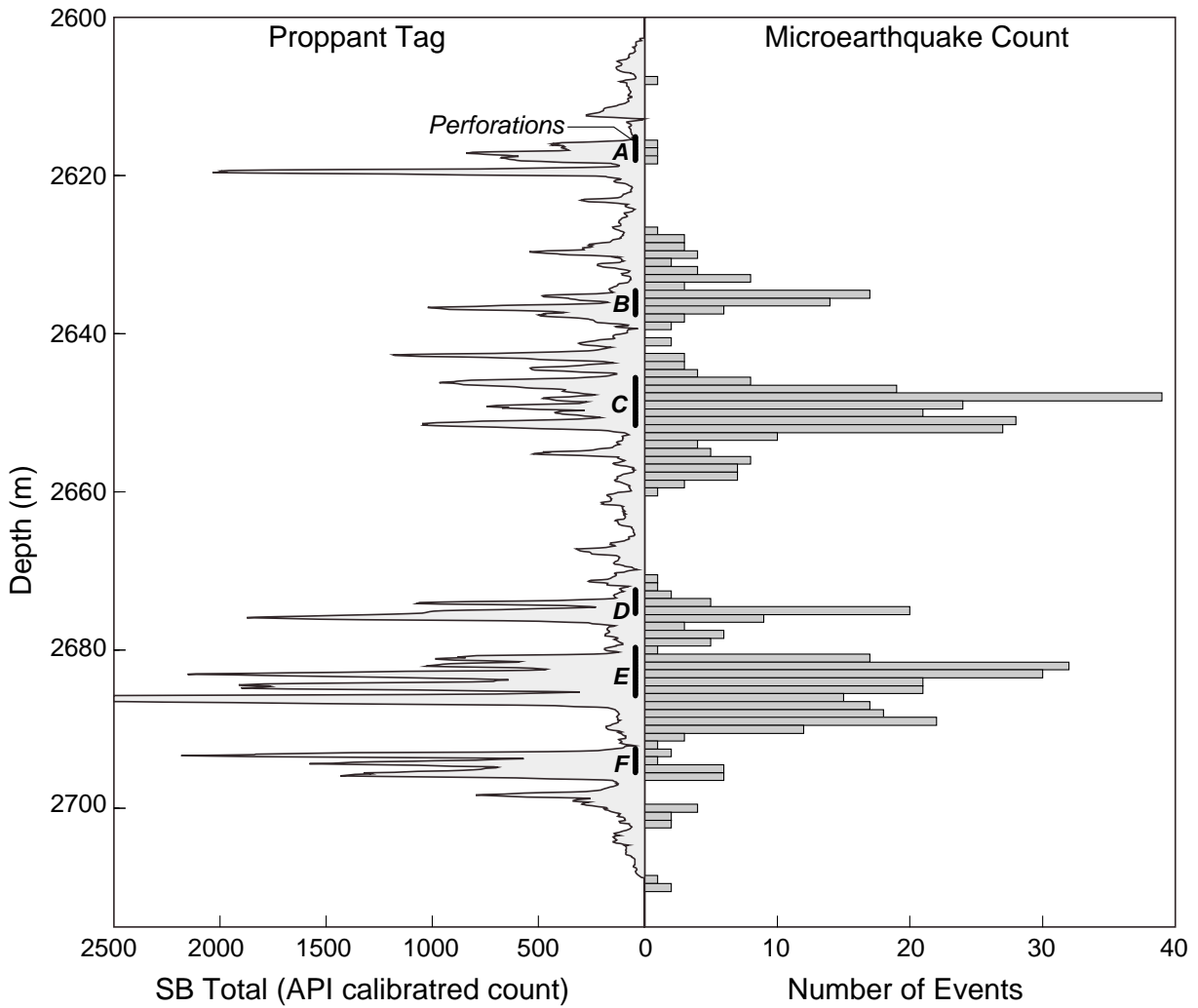


Fig. 13. The depth distribution of microearthquakes within the Stage-3 treatment interval of Figure 10 compared to the radioactive (RA) proppant tracer log. The dark vertical lines labeled **A** through **F** mark the Stage-3 perforation zones of the treatment well 21-10. The RA proppant tag was antimony (SB).

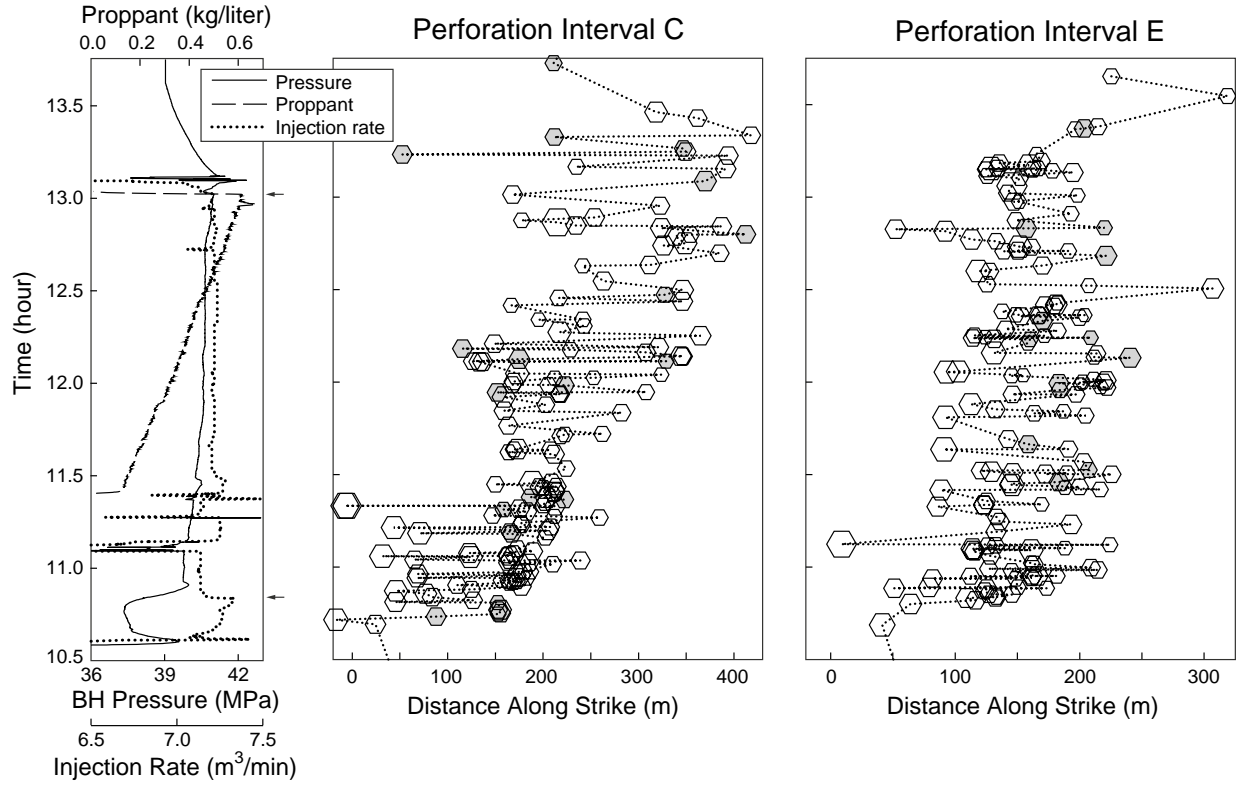


Fig. 14. Fracture growth for the two most populous seismicity clusters associated with perforation intervals **C** and **E** of Figure 13. Symbol sizes are proportional to magnitudes (log-amplitudes). Open and gray symbols distinguish events fitting the left-lateral and right-lateral strike-slip focal mechanisms, respectively. The two arrows mark the interval when the crosslink gel was being injected. Distance along strike represents the eastern wing of the seismicity with the treatment well at zero. Note that the distance scales differ for the two perforation intervals.

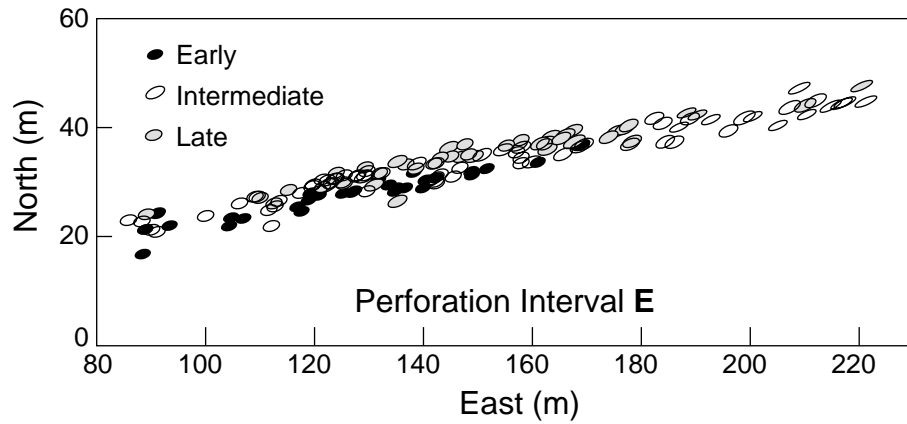


Fig. 15. Detailed map view of the subcluster associated with perforation interval **E** of Figure 13. Only events with RMS residuals ≤ 0.35 ms are displayed. Locations are represented by the projections of the error ellipsoids. The symbol type represent a coarse time division in the treatment schedule.

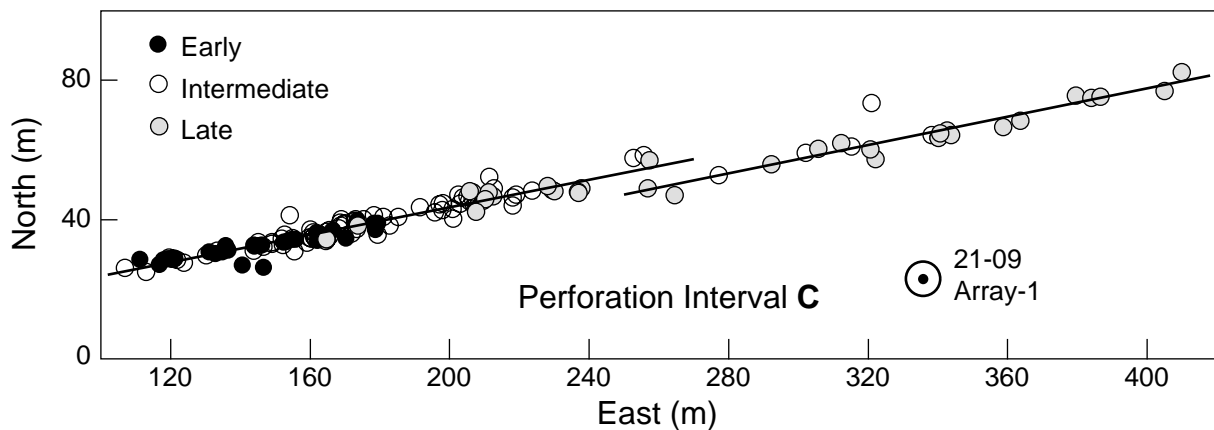


Fig. 16. Detailed map view of the subcluster associated with perforation interval **C** of Figure 13. Only events with RMS residuals ≤ 0.35 ms are displayed. The symbol type represents the same time sequence as Figure 15. The parallel lines shown on each side of the trend offset near 250 m east are best-fit linear regressions for events < 250 m and > 250 m east.